

Powerful yet lonely: Is 3C 297 a high-redshift fossil group?

VALENTINA MISSAGLIA,^{1,2,3} JUAN P. MADRID,⁴ MISCHA SCHIRMER,⁵ FRANCESCO MASSARO,^{1,2,3}
ALBERTO RODRÍGUEZ-ARDILA,^{6,7} CARLOS J. DONZELLI,⁸ MARTELL VALENCIA,⁴ ALESSANDRO PAGGI,^{1,2,3}
RALPH P. KRAFT,⁹ CHIARA STUARDI,^{10,11} AND BELINDA J. WILKES^{9,12}

¹*Dipartimento di Fisica, Università degli Studi di Torino, via Pietro Giuria 1, I-10125 Torino, Italy*

²*INFN-Istituto Nazionale di Fisica Nucleare, Sezione di Torino, I-10125 Torino, Italy.*

³*INAF-Osservatorio Astrofisico di Torino, via Osservatorio 20, I-10025 Pino Torinese, Italy*

⁴*Departamento de Física y Astronomía, La Universidad de Tejas en el Valle del Río Grande, Brownsville, TX 78520, USA*

⁵*Max-Planck-Institut für Astronomie, Königstuhl 17, D-69117 Heidelberg, Germany*

⁶*LNA/MCTIC, Rua dos Estados Unidos, 154. Bairro das Nações, Itajubá, MG B-37501-591, Brazil*

⁷*Divisão de Astrofísica, INPE, Avenida dos Astronautas 1758, São José dos Campos, B-12227-010 SP, Brazil*

⁸*Instituto de Astronomía Teórica y Experimental IATE, CONICET – Observatorio Astronómico, Universidad Nacional de Córdoba, Laprida 854, X5000BGR, Córdoba, Argentina*

⁹*Center for Astrophysics, Harvard & Smithsonian, 60 Garden Street, Cambridge, MA 02138, USA*

¹⁰*Dipartimento di Fisica e Astronomia, Università di Bologna, via Gobetti 93/2, I-40129 Bologna, Italy*

¹¹*INAF - Istituto di Radioastronomia di Bologna, Via Gobetti 101, I-40129 Bologna, Italy*

¹²*School of Physics, University of Bristol, Bristol, UK*

ABSTRACT

The environment of the high-redshift ($z = 1.408$), powerful radio-loud galaxy 3C 297 has several distinctive features of a galaxy cluster. Among them, a characteristic halo of hot gas revealed by Chandra X-ray observations. In addition, a radio map obtained with the Very Large Array (VLA) shows a bright hotspot in the northwestern direction, created by the interaction of the AGN jet arising from 3C 297 with its environment. In the X-ray images, emission cospatial with the northwestern radio lobe is detected, and peaks at the position of the radio hotspot. The extended, complex X-ray emission observed with our new Chandra data is largely unrelated to its radio structure. Despite having attributes of a galaxy cluster, no companion galaxies have been identified from 39 new spectra of neighboring targets of 3C 297 obtained with the Gemini Multi-Object Spectrograph. None of the 19 galaxies for which a redshift was determined lies at the same distance as 3C 297. The optical spectral analysis of the new Gemini spectrum of 3C 297 reveals an isolated Type-II radio-loud AGN. We also detected line broadening in [O II] $\lambda 3728$ with a FWHM about 1700 km s^{-1} and possible line shifts of up to $500\text{--}600 \text{ km s}^{-1}$. We postulate that the host galaxy of 3C 297 is a fossil group, in which most of the stellar mass has merged into a single object, leaving behind an X-ray halo.

Keywords: Active galactic nuclei (16) – Brightest Cluster Galaxies (181) – Galaxy clusters (584) – Intracluster medium (858)

1. INTRODUCTION

The sample of powerful radio sources in the Third Cambridge Revised Catalog (3CR; Bennett et al. 1962a,b) has served for decades as the foundation to investigate the nature and evolution of radio-loud active galactic nuclei (AGN; see Merloni & Heinz 2013, for a review). There is consensus that strong extragalac-

tic radio sources are at the core of massive elliptical galaxies, powered by supermassive black holes (SMBH) (Rees 1984; Begelman et al. 1984). Radio-loud AGN launch bright, powerful plasma jets (e.g. Salpeter 1964; Lynden-Bell 1969; Padovani et al. 2017; Blandford et al. 2019) that typically extend over scales much larger than the host galaxy itself, interacting with – and sometimes shaping – the surrounding intracluster medium (ICM). This phenomenon, known as feedback (see e.g., Fabian 2012), can also ignite or quench star formation. An iconic example is M87 (3C 274; Owen et al. 2000; Chu-

razov et al. 2001; Forman et al. 2007; de Gasperin et al. 2012; Perley & Meisenheimer 2017), whose SMBH has recently been directly imaged (Event Horizon Telescope Collaboration 2019).

Some of these powerful radio sources are typically the most luminous members of the galaxy cluster in which they reside, being therefore called Brightest Cluster Galaxies (BCGs; Best et al. 2007), usually fed by “cooling flows” (e.g. Fabian 2012; Bykov et al. 2015).

At high redshift ($z > 1$), some of these radio sources act as beacons indicating the potential presence of galaxy clusters whose members have not been yet identified (e.g. Wing & Blanton 2011; Paterno-Mahler et al. 2017). In particular, at redshift ~ 2 , it is possible to study the epoch of galaxy cluster formation, to understand how the ICM properties evolve and how this can affect cluster formation and evolution (see e.g. Rosati et al. 2002, and references therein).

The work presented here focuses on 3C 297, a radio-loud quasar at $z = 1.406$ (Spinrad et al. 1985), and suggests the presence of a massive cluster in formation. Spinrad et al. (1985) emphasized the high redshift of 3C 297, and reported the detection of [Mg II], [Ne IV], and [C III] lines in its spectrum. Jackson & Rawlings (1997) took a near-infrared spectrum of 3C 297 between 1.05 and 1.25 μm , detecting a prominent [O III] $\lambda 5007$ line redshifted to 1.2053 μm corresponding to a redshift measurement $z = 1.407$.

This source has a large suite of recent multiwavelength observations. Chiaberge et al. (2015) classify 3C 297 as a merger, using Hubble Space Telescope (*HST*) observations, because of the presence of a double core. Hilbert et al. (2016) reported earlier radio, optical, and infrared observations of 3C 297. A Very Large Array (VLA) map shows a strong, straight lobe of radio emission stretching from the host galaxy to more than $5''$ (~ 43 kpc) to the northwest. In addition, 3C 297 has diffuse radio emission to the south of the host galaxy. The southern radio emission includes two knots of optical emission, whose relative position is uncertain given the absence of a radio core to align the radio and the optical/IR. From observations obtained with the UVIS channel of *HST*’s Wide Field Camera 3 through the F606W filter and with the IR channel through the F140W filter, 3C 297 appears as a compact but resolved core with diffuse emission, with an arc $2''$ north of the core and a highly elongated source $1''$ to the south. This highly elongated source is suggestive of a recent/ongoing merger as already claimed by Chiaberge et al. (2015).

Kotyla et al. (2016) analyzed *HST* data of 21 high- z sources of the 3C catalog and noticed that 3C 297 lacks an associated galaxy cluster or group.

In the Chandra Snapshot Survey of 3C sources (Massaro et al. 2015, 2018; Stuardi et al. 2018), 3C 297 shows a complex morphology of its X-ray halo as the likely result of an interaction with the radio jet (“feedback”, see e.g. Fabian 2012; Kraft et al. 2012).

The combination of multiobject spectroscopy and Chandra data proved to be an efficient method to find that another 3C source belongs to a galaxy cluster. In Madrid et al. (2018) we used Gemini spectra and Chandra images to identify a previously unknown cluster of galaxies around 3C 17, at $z = 0.22$. 3C 17 has been of particular interest because its radio jet is dramatically bent (Morganti et al. 1999; Massaro et al. 2009, 2010), a sign of strong interaction with the ICM.

While the presence of hot gas and the bent radio jet of 3C 297 are typical for galaxy clusters, no galaxies at the same redshift are known in the literature around 3C 297 within ~ 2 Mpc. These findings prompted us to do follow-up observations of 3C 297 in an effort to find potential companions.

In this paper, we present new Gemini multiobject spectroscopy of field galaxies in the vicinity of 3C 297, to search for a potential galaxy group or cluster members, and new Chandra observations performed to distinguish between the X-ray emission arising from the ICM and that related to the large-scale radio structure.

In Section 2, we describe the Chandra data reduction and analysis. In Section 3, we describe our new Gemini observations. Section 4 is devoted to the analysis of Gemini optical spectra. In Section 5, we discuss the possibility that 3C 297 may be the central galaxy of a fossil group. A brief summary and our conclusions are given in Section 6. Throughout the paper we assume a Λ CDM cosmology with $H_0 = 69.6 \text{ km s}^{-1} \text{ Mpc}^{-1}$, $\Omega_M = 0.286$, and $\Omega_\Lambda = 0.714$ (Bennett et al. 2014).

2. CHANDRA OBSERVATIONS, DATA REDUCTION AND ANALYSIS

3C 297 was observed by *Chandra* in 2016 as part of the 3C Snapshot Survey (see Stuardi et al. 2018, for a recent review) for a total exposure of ~ 12 ks (OBSID: 18103).

New Chandra ACIS-S data in VERY FAINT mode (P.I. Missaglia) were obtained between 2021 April and 2022 April (see Figure 1). The awarded observing time has been divided into 10 observations, for a total nominal exposure time of ~ 200 ks (OBSIDs: 23829; 24352, 24353, 24355, 24356, 24357, 25000, 25001, 25004, 25023). *Chandra* data reduction was carried out using the Chandra Interactive Analysis of Observations (CIAO v4.13 Fruscione et al. 2006) following standard

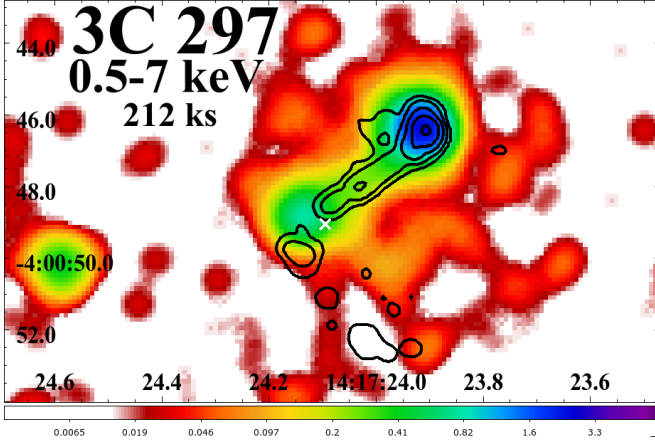


Figure 1. *Chandra* image of 3C 297, obtained after merging the available observations, for a total of 212 ks. The image has been filtered in the energy range 0.5–7 keV, binned with a pixel size of $0.123''/\text{pixel}$ and smoothed with a $3.44''$ Gaussian kernel. VLA 8.4 GHz (restoring beam $0.357'' \times 0.233''$) black radio contours are drawn starting at $0.08 \mu\text{Jy beam}^{-1}$, increasing by factors of six. The position of the radio core, derived from the spectral index map, is marked with a white cross.

procedures and threads¹, and the Chandra Calibration Database (CALDB) version 4.9.6. Level 2 event files were created using the CIAO task `chandra_repro`. We removed flares from lightcurves², and astrometrically registered all the images using the VLA 8.4 GHz radio observation, smoothing the X-ray observations to find the brightest pixel corresponding to the northern hotspot as in the VLA image. This association is permissible within the astrometric uncertainties of both data sets. The VLA data we use was obtained in the A configuration (maximum baseline 36 km) on 1990 May 10 at 8.44 GHz.

Stuardi et al. (2018) suggested a tentative position of the radio core, based on the results of the spectral index map. However, to register the X-ray images, we used the northern hotspot because it is a bright feature, easy to recognize. As a last step, we merged all the observations³ for the spectral analysis of the most interesting features.

The spectral analysis focused on three distinct areas with sufficient counts: the northern hotspot, the extended region, and the nucleus (see Figure 2). Before this, we extracted the surface brightness profiles in four directions (see Figure 3) choosing sections with an

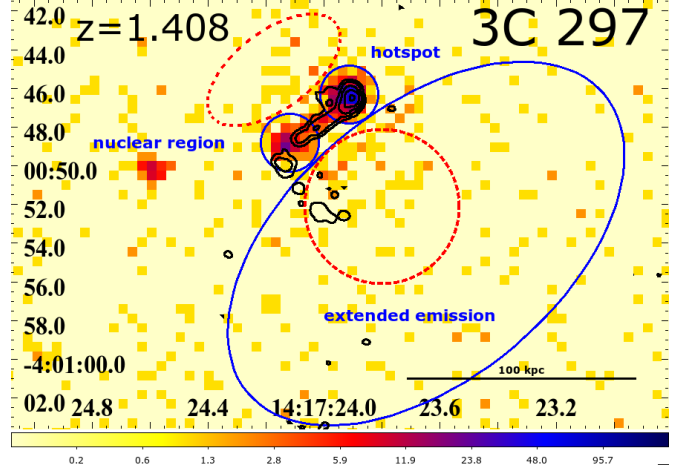


Figure 2. Unbinned, unsmoothed *Chandra* merged image of 3C 297 in the energy band 0.3–7 keV. The three regions in which spectral analyses have been performed are highlighted in the blue regions (two circles and one ellipse). We detected 159 net counts in the extended emission region, 115 net counts in the nuclear region and 315 net counts in the hotspot region. The red dashed circle and ellipse mark the regions in which we observe an X-ray counts excess, due to the outflow (see Section 4.3 for more details).

outer radius of $30''$ and a signal-to-noise ratio of 3 in each radial bin. We then extracted the spectra with the `specextract`⁴ script and performed the fitting with Sherpa (Freeman et al. 2001).

We extracted the spectrum of the hotspot within a circular aperture of $\sim 1.5''$ diameter in the reprojected observation, and we extracted the spectrum merging the 11 available observations (snapshot plus new observations). Adopting a model with Galactic absorption and a power law (`xstabs.absgal*xspowerlaw.pl`) setting the Galactic absorption to the value of $3.49 \times 10^{20} \text{ cm}^{-2}$, as reported in HI4PI Collaboration et al. (2016), we obtained a photon index $\Gamma = 1.8 \pm 0.16$ and an X-ray luminosity of the hotspot $L_X = 2.82^{+0.57}_{-0.46} \times 10^{44} \text{ erg s}^{-1}$ between 0.5 and 7 keV.

We performed the spectral analysis of the extended emission in the southwestern direction. We extracted spectra from an elliptical region (see Fig. 2) with semi-major and minor axes of $12''$ and $7''$, respectively. The axes were selected based on the surface brightness profile in the southwestern direction.

To investigate if this emission is non thermal, due to inverse Compton scattering (IC) of non-thermal radio-emitting electrons on cosmic microwave background (CMB) photons (IC/CMB; Felten & Rees 1969; Cooke

¹ <http://cxc.harvard.edu/ciao/threads/>

² <https://cxc.harvard.edu/ciao/ahelp/deflare.html>

³ https://cxc.harvard.edu/ciao/ahelp/reproject_obs.html

⁴ <https://cxc.cfa.harvard.edu/ciao/ahelp/specextract.html>

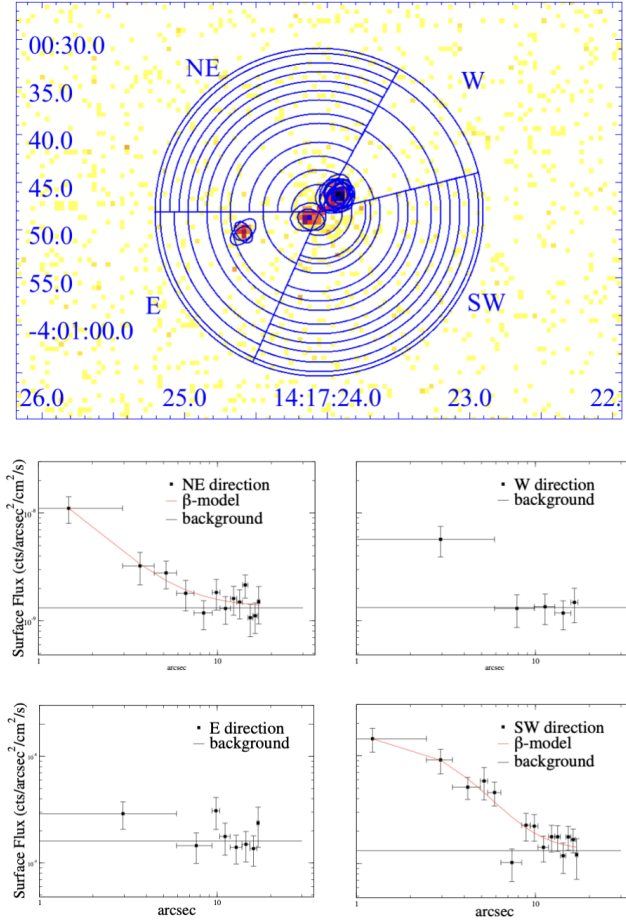


Figure 3. *Top Panel:* Merged *Chandra* X-ray image (0.5–7 keV) showing the annuli used to extract surface brightness profiles in four sectors. Blue ellipses represent the point sources excluded from each observation before merging the separate pointings. The source in the eastern region is unrelated. *Bottom Panel:* Surface brightness profiles for the regions highlighted in the top panel. In the western and eastern directions the emission cannot be fitted with a β -model.

et al. 1978; Harris & Grindlay 1979), or thermal, and therefore related to the ICM, we adopted two different models for the extended emission: (1) Galactic absorption plus a power law (`xswabs.absgal*xspowerlaw.pl`), and (2) Galactic absorption plus a thermal model (`xswabs.absgal*xsapec.therm`).

As reported in the literature (see e.g. Massaro & Ajello 2011; Ghisellini et al. 2015, and references therein), the magnetic fields in the lobes of radio galaxies are relatively low, of the order of tens of microgauss, therefore radiating synchrotron emission inefficiently.

At high z the CMB energy density dominates the radio-lobe magnetic field energy density. Therefore, as described by Ghisellini et al. (2014 a,b, and references

therein; see also Volonteri et al. 2011), at high z the high-energy electron population is depleted due to scattering on the CMB photons, which serves to reduce the radio brightness of the lobes (CMB quenching). At the same time, the increased CMB energy density, enhances the IC/CMB X-ray emission from the lobes (Rees et al. 1968).

Yuan et al. (2003) presented a *Chandra* analysis of the extended X-ray emission around the high-redshift ($z=4.301$) quasar GB1508+5714. This emission is well described as IC/CMB, and the lack of an obvious detection of radio emission from the extended component could be a consequence of Compton losses on the electron population, or of a low magnetic field. It is also argued that extended X-ray emission produced by IC scattering may be common around high-redshift radio galaxies and quasars, demonstrating that significant power is injected into their surrounding by powerful jets.

In the nonthermal scenario (X-ray diffuse emission due to IC/CMB in the lobes), we obtained a photon index equal to $\Gamma = 2.72^{+0.94}_{-0.77}$ and a luminosity of $L_X = 6.6^{+3.3}_{-2.5} \times 10^{43} \text{ erg s}^{-1}$ (see details in Table 1).

Given that the diffuse X-rays are not associated with the radio structure, we also had to consider the thermal scenario (X-ray emission from the ICM), even if in the case of cluster emission we should expect a spherically symmetric emission. In this case, adopting a (`xswabs.absgal*xsapec.therm`) model, we could only put an upper bound on the temperature of 6 keV. This translates to an X-ray luminosity between 0.5 and 7 keV of $L_X = 4.5^{+2.0}_{-1.7} \times 10^{43} \text{ erg s}^{-1}$ ($\chi^2(\text{dof})=0.72(6)$). To disentangle the two scenarios, we would need low-frequency radio data that could trace the extension of the southern lobe and allow us to estimate the IC/CMB contribution to the X-ray emission from the lobe region.

Finally, we extracted the spectrum of the nuclear region, i.e. the region that in the optical corresponds to the host galaxy of 3C 297 (the position of the central AGN identified with the radio spectral index map as reported in Stuardi et al. (2018) that is marked with a white cross in Fig. 1). We adopted a model with Galactic and intrinsic absorption, plus a power law (`xswabs.absgal*xszwabs.absint*xspowerlaw.pl`). We fitted the spectrum in three different configurations: (1) with photon index, normalization, and intrinsic absorption as free parameters; (2) with photon index equals 1.8 and free intrinsic absorption and normalization, and (3) with no intrinsic absorption. Results of the spectral fitting for the three components are summarized in Table 1. The nucleus has an X-ray luminosity of $L_X = 1.15^{+0.53}_{-0.40} \times 10^{44} \text{ erg s}^{-1}$ between 0.5–7 keV.

Results of the X-Ray spectral fitting					
Region	Power-Law				
	$N_{H,int}$ (10^{22} cm^{-2})	Γ	norm (10^{-6} cm^{-5})	$\chi^2_{\nu}(\text{dof})$	$L_{X(0.5-7\text{keV})}$ ($10^{44} \text{ erg s}^{-1}$)
Northern Hotspot	-	1.87 ± 0.15	$4.87^{+0.65}_{-0.22}$	0.68(13)	$2.82^{+0.57}_{-0.46}$
X-ray Halo	-	$2.72^{+0.94}_{-0.77}$	$1.50^{+0.58}_{-0.54}$	0.63(6)	$0.66^{+0.33}_{-0.25}$
Nucleus	1.95×10^{-4}	$1.44^{+0.51}_{-0.31}$	$1.42^{+1.27}_{-0.37}$	0.42(2)	
	>4.7	1.8*	$2.16^{+0.51}_{-0.45}$	0.48(3)	$1.15^{+0.53}_{-0.40}$
	-	$1.44^{+0.33}_{-0.31}$	$1.42^{+0.46}_{-0.39}$	0.28(5)	
Region	Thermal				
	$N_{H,int}$ (10^{22} cm^{-2})	kT (keV)	norm (10^{-6} cm^{-5})	$\chi^2_{\nu}(\text{dof})$	$L_X(0.5-7\text{keV})$ ($10^{43} \text{ erg s}^{-1}$)
X-ray Halo	-	<6	25^{+34}_{-13}	0.72(6)	$4.5^{+2.0}_{-1.7}$

Table 1. Results of the spectral fitting of the X-Ray components: northern hotspot, extended emission and nucleus (all highlighted in Fig. 2). * marks fixed values in the fit.

3. GEMINI OBSERVATIONS

3.1. Preimage and Target selection

For field spectroscopy, we used the Gemini Multi-Object Spectrograph (GMOS; Hook et al. 2004). The *i*-band preimage for the mask design was obtained on 2020 February 18 through program GS-2019B-FT-211 (PI: Madrid) with GMOS at Gemini South. The integration time was 1080 s, taken in clear and $0.75''$ seeing conditions.

In our GMOS *i*-band preimage (see Figure 4), 3C 297 has an *i*-band magnitude of 20.7 AB mag. Lacking photometric redshifts in the field, our initial target selection was based on the *i*-band photometry of galaxies in this image. If there was a galaxy cluster around 3C 297, then most members would be considerably fainter than the BCG – in the case of a fossil group, by at least 2.5 mag within the virial radius (Dariush et al. 2007). We therefore selected our high-priority target sample from the $21.8 < i < 23.0$ AB mag interval, corresponding to $0.2\text{--}3.0 \times 10^{10} L_{\odot}$ if at $z \sim 1.4$. The bright cutoff was chosen to reduce the contamination by foreground sources. For targets below the faint cutoff it would be increasingly difficult to determine a spectroscopic redshift, in particular if they reside in the redshift desert between $z \sim 1.8\text{--}2.5$, where redshifted emission lines are absent in the optical wavelength range. Galaxies with $i = 23.0\text{--}24.0$ mag comprised a low-priority sample that the mask-making algorithm could use to fill any remaining spaces in the mask design.

After the Gemini mask-making software automatically resolved slit-placement conflicts (spatial or spectral overlaps), 40 galaxies – or about 50% of the targets – remained in the mask design. Science targets had slitlets of $1''$. While this sample of 40 targets is necessarily in-

complete, it is still representative, enabling us to detect a potential cluster population in the spatial vicinity of 3C 297. In addition to these galaxies, we had two alignment stars in wider slits, and one reference star and three galaxies of similar brightness as 3C 297 in narrow science slits, to guide the data processing and judge data quality. 3C 297 was also included, near the center of the mask (see Table 2 and Figure 4).

3.2. Band-shuffling mask design

We used GMOS in its band-shuffling mode, which allows for very high slit density in a fairly compact area. Specifically, one-third of the detector area or $5.5' \times 1.8'$ are available for the slit placement, corresponding to a projected physical area of 2.8×0.9 Mpc at $z = 1.408$.

During the observations, science targets are observed for 60 s, after which the collected charges are moved (“shuffled”) to an unilluminated detector area, and the telescope makes a small offset. During the next 60 s, at the offset position, the slits collect sky signal only. Then the *target* charges are shuffled back under the slit, and the sky charges are moved onto a different storage area. This is repeated for a total of 600 s in a single exposure, for an effective on-source integration time of 300 s. Very accurate sky subtraction and fringe correction becomes possible at longer wavelengths dominated by airglow, with just a single readout, and redshifts can be secured for fainter galaxies. For details about this mode see Glazebrook & Bland-Hawthorn (2001).

3.3. Instrumental setup

Our instrumental setup is optimized to identify galaxies at a redshift of $z \sim 1.4$. Many characteristic emission lines of active and star-forming galaxies, such as [MgII] λ 2799, [OII] λ 3727, [NeIII] λ 3869, and H δ , would be redshifted to the 670–990 nm range. This interval

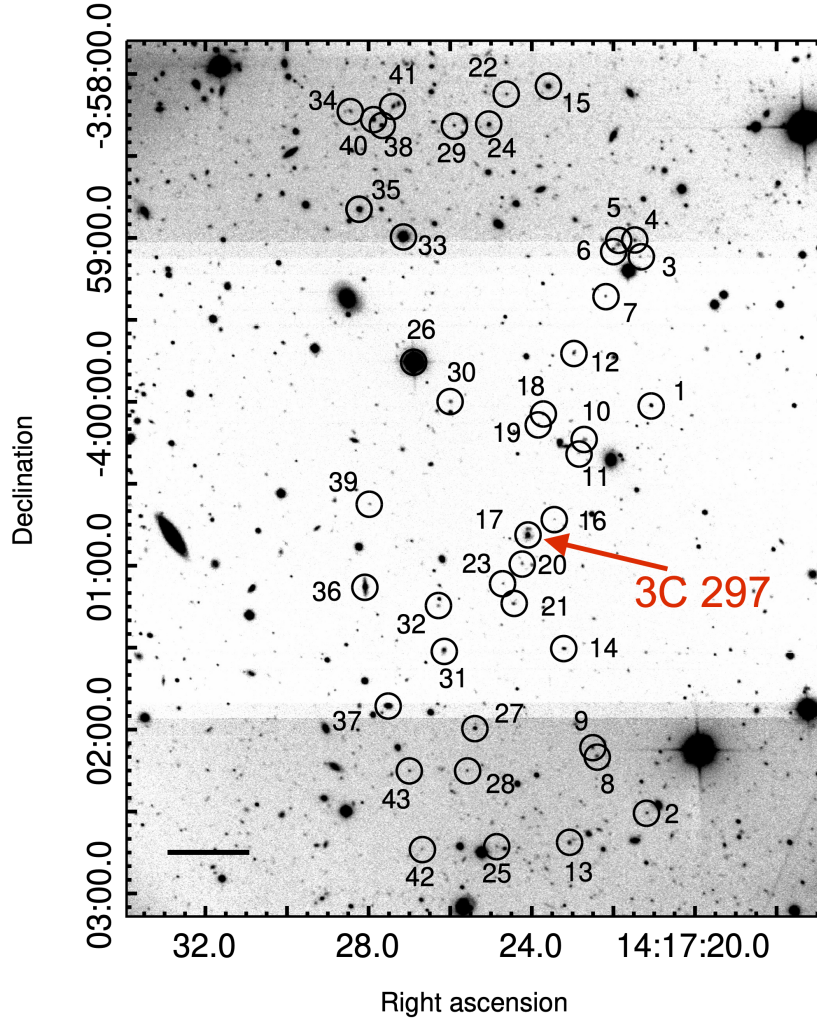


Figure 4. Section of the GMOS preimage of the 3C 297 field. This i -band image has a total exposure time of 1080 s. Numbers correspond to the slit ID. The radio galaxy 3C 297 is close to the center of the image, identified with slit number 17. The bar on the lower left represents $30''$. The different background levels are a due to limited processing functionality by the Gemini pipeline that automatically produces the preimage. North is up and east is left.

then also includes the characteristic Balmer break and the Ca H+K absorption lines of older stellar populations in elliptical galaxies. Our instrumental setup for GMOS, therefore, used the R400 grating with the OG515 order-sorting filter and a central wavelength of 790 nm. The associated spectral resolution for a slit width of $1''$ is $R = 960$. The main observable wavelength interval with this setup was 510–1050 nm, with negligible second-order overlap above 1020 nm. Depending on how close a source was located to the edge of the masking area, the spectral range was truncated by the detector edges either at the blue or the red end. Typically, we cov-

ered a 450 nm wide interval within 510–1050 nm for each source.

3.4. Observations

One month after our original mask was cut and tested, Gemini suspended its science operations due to the pandemic, preventing our program to proceed with the spectral observations. By the time Gemini South reopened, the GMOS-S detector was experiencing considerable charge-transfer efficiency issues that were prohibitive for our band-shuffling observations.

The mask was thus redesigned for identical band-shuffling observations with GMOS-N at Gemini North,

using the GMOS-S preimage. Spectra were obtained on 2021 April 13 and 15 under program GN-2021A-FT-203 (PI: Madrid), with an effective on-source integration time of $11 \times 300 = 3300$ s, and an image seeing of $0.5''$ – $0.8''$. We binned the detector 2×2 (in the spatial and spectral dimensions), and observed two central wavelength settings of 790 nm and 800 nm to cover the detector gaps. Calibration data consisted of biases, lamp and twilight flats, and CuAr arc spectra for wavelength calibration.

3.5. Data reduction

The data reduction was carried out following a sequence of PYRAF Gemini/GMOS routines. Biases and flat-fields were reduced using the tasks GBIAS and GSFLAT. Spectra for science targets and the CuAr lamps were processed with the GSREDUCE task. The GSWAVELENGTH routine was used to derive the wavelength calibration from the CuAr frames that were applied to the science spectra with GSTRANSFORM. Sky subtraction was performed with GNSSKYSUBTRACT and final 1-D spectra extraction was carried out with the routine GSEXTRACT.

Flux calibration was achieved using GMOS longslit observations of the spectroscopic standard star *Feige66* made during the observing run. All spectra were flux calibrated and extinction corrected with the GSCALIBRATE task. Lastly, we combine all 1D spectra into a single spectrum for each target using GEMCOMBINE.

4. ANALYSIS OF THE OPTICAL SPECTRA

4.1. 3C 297

Our GMOS spectrum of 3C 297 is displayed in Fig. 5. This spectrum has prominent emission lines: Mg II, O III, He II, [Ne V], [O II], and [Ne III]. From the position of the different lines, we measured a mean redshift of $z=1.408 \pm 0.001$.

Before undertaking our detailed spectral analysis, we applied a redshift correction of $z=1.408$ to the spectrum of 3C 297. We also applied a Galactic extinction correction of $A_{\lambda,V}=0.146$ mag using the extinction maps of Schlafly et al. (2011) and the Cardelli et al. (1989) extinction law. In order to increase the signal-to-noise (S/N) of the emission lines, we smoothed the spectrum using a Gaussian filter of 3 pixels width. This smoothing preserves the spectral resolution while suppressing high-frequency noise.

The spectrum of 3C 297 is essentially free of either blue or red continuum emission. Moreover, we do not detect stellar absorption features. The presence of Mg II 2798 Å

Table 2. Targets of the GMOS multi-slit mask

Slit	R.A.	Dec.	m_i	z
1	14:17:21.076	-4:00:01.45	21.45	—
2	14:17:21.177	-4:02:30.65	23.37	—
3	14:17:21.344	-3:59:07.30	23.91	☆
4	14:17:21.475	-3:59:01.19	22.92	—
5	14:17:21.871	-3:59:02.67	22.96	—
6	14:17:22.008	-3:59:04.24	23.01	1.156
7	14:17:22.193	-3:59:21.65	23.26	0.633
8	14:17:22.400	-4:02:09.94	23.09	1.263
9	14:17:22.525	-4:02:06.74	22.87	1.163
10	14:17:22.737	-4:00:14.41	22.68	1.029
11	14:17:22.855	-4:00:19.08	23.81	—
12	14:17:22.977	-3:59:42.29	22.51	1.523
13	14:17:23.077	-4:02:41.65	22.63	—
14	14:17:23.204	-4:01:30.48	22.28	—
15	14:17:23.588	-3:58:04.49	21.23	0.215
16	14:17:23.455	-4:00:43.17	24.25	—
17	14:17:24.102	-4:00:48.93	20.95	1.408
18	14:17:23.719	-4:00:04.45	22.74	—
19	14:17:23.839	-4:00:08.48	23.22	1.137
20	14:17:24.232	-4:00:59.38	23.21	—
21	14:17:24.447	-4:01:14.20	22.89	—
22	14:17:24.621	-3:58:07.42	23.44	1.343
23	14:17:24.702	-4:01:06.75	23.57	1.577
24	14:17:25.052	-3:58:18.53	21.91	—
25	14:17:24.861	-4:02:43.03	23.80	—
26	14:17:26.898	-3:59:45.86	15.12	☆
27	14:17:25.387	-4:01:59.64	21.88	—
28	14:17:25.583	-4:02:15.24	23.56	0.732
29	14:17:25.901	-3:58:18.92	23.10	2.577
30	14:17:25.989	-4:00:00.01	22.87	—
31	14:17:26.160	-4:01:30.80	21.69	0.211
32	14:17:26.292	-4:01:14.94	23.35	1.181
33	14:17:27.150	-3:58:59.79	17.44	☆
34	14:17:28.444	-3:58:13.55	23.12	—
35	14:17:28.238	-3:58:49.56	20.34	—
36	14:17:28.087	-4:01:07.61	20.20	—
37	14:17:27.513	-4:01:51.40	20.38	0.244
38	14:17:27.675	-3:58:18.69	21.72	0.295
39	14:17:27.965	-4:00:37.53	23.32	—
40	14:17:27.882	-3:58:16.70	21.41	0.605
41	14:17:27.389	-3:58:12.06	22.42	—
42	14:17:26.692	-4:02:43.83	23.98	1.199
43	14:17:27.001	-4:02:15.24	23.37	—

NOTE—Column 1: Slit number; Column 2: Right Ascension (J2000); Column 3: Declination (J2000); Column 4: apparent i -band magnitude; Column 5: redshift. Slits 3, 26, and 33 are stars denoted with the ☆ symbol. 3C 297 (slit 17) is highlighted in boldface.

and [Ne V] $\lambda\lambda 3345, 3424$ is further proof of the AGN nature of this object. The latter doublet is conspicuous, suggesting that 3C 279 has high-ionization gas.

The strongest line detected in the observed wavelength interval corresponds to [O II] $\lambda\lambda 3726, 3729$ (hereafter [O II] $\lambda 3728$). This line profile displays a broad, prominent blue asymmetry, indicating the presence of powerful outflows in the center of the radio galaxy. In

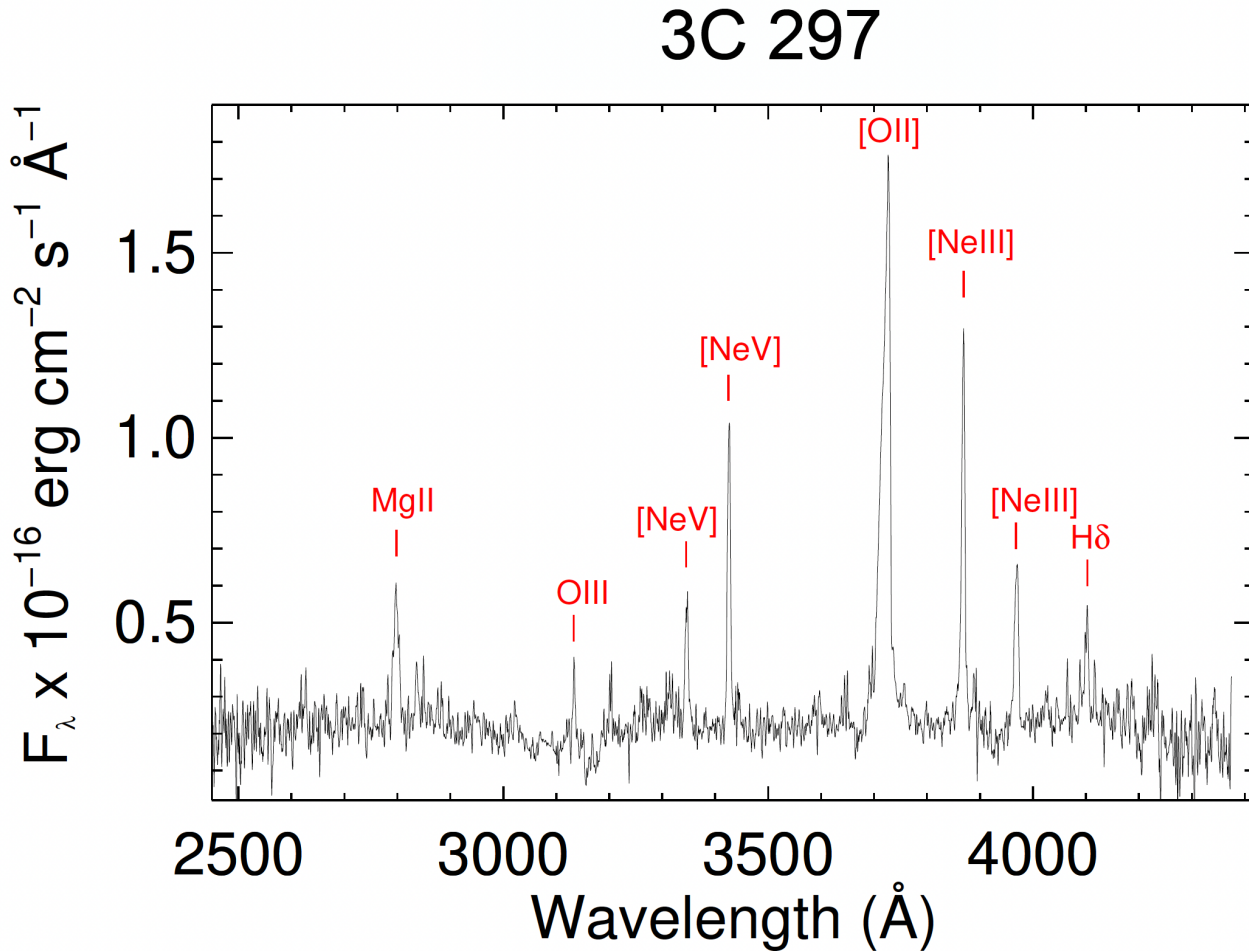


Figure 5. New GMOS spectrum of 3C 297. The spectrum is displayed with a redshift correction of $z=1.408$.

blue-asymmetric oxygen lines a component is usually shifted to the blue by a few hundred km/s or more, relative to the systemic velocity and is significantly broader than the narrower component. In some quasars, this blueshifted line can display FWHM values of a few thousand kilometers per second and the centroid of the line can be shifted by several hundred kilometers per second relative to the systemic velocity (see Zakamska & Greene (2014) and discussion below).

In order to measure the flux, centroid position, and FWHM of the emission lines, we fitted Gaussian functions to individual lines, or to sets of blended lines, using PYTHON scripts written by our team. Usually, one or two Gaussian components were used to reproduce the observed profile. The criterion for the best solution was the minimum value of the reduced χ^2 .

Typically, one Gaussian is needed to properly fit the observed lines except for [O II], where two components were used. Throughout this process, the underlying con-

tinuum emission was approximated by a linear fit. Figure 6 shows examples of the Gaussian fitting for [Ne V] and [O II]. Table 3 lists the integrated emission line fluxes of all lines measured at a 3σ level, the centroid position, and the FWHM. Notice that all lines except Mg II and [O II] broad are spectroscopically unresolved (the instrumental FWHM is 6.8 Å.)

4.2. The AGN activity in 3C 297

The continuum emission in 3C 297 has no hints of either a blue continuum, typical of Type I AGN, or stellar absorption features, usually observed in Type II AGN. However, the detection of coronal lines of [Ne V], usually associated with AGN, confirms the presence of an active nucleus in this object (see Figure 5).

We searched for the presence of broad-line features indicative of a broad-line region (BLR). The only permitted lines, detected at a 3σ level, are those of Mg II $\lambda 2798$, O III $\lambda 3133$ and H δ at 4101 Å (see Fig. 5). The former is

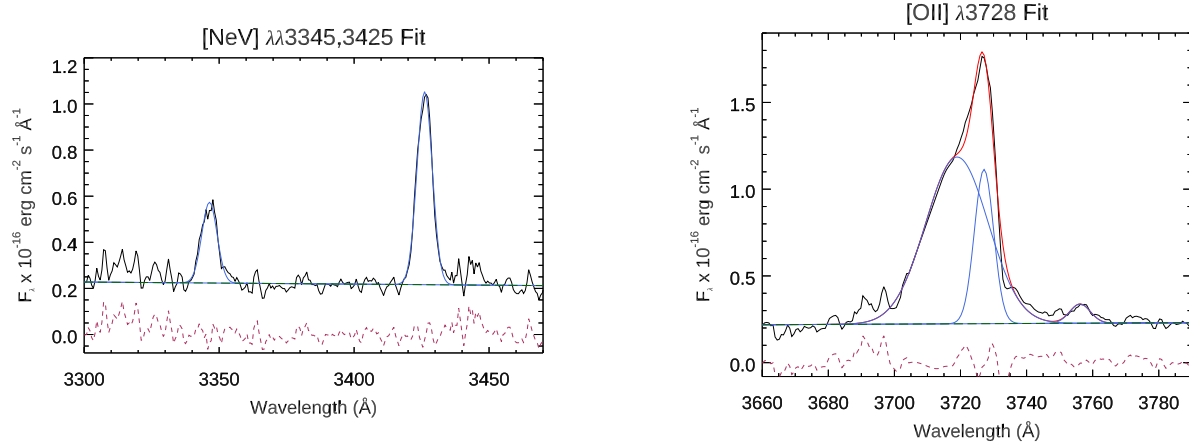


Figure 6. Example of the Gaussian decomposition applied to the observed emission line profiles. *Left:* Fit to the coronal lines [Ne V] $\lambda\lambda$ 3345, 3425. *Right:* [O II] $\lambda\lambda$ 37286, 3729. For this latter line, a second blueshifted, broad component of $\text{FWHM}=1790 \text{ km s}^{-1}$ was necessary to reproduce the observed profile. In both panels, the observed profile is in black, individual Gaussians are in blue, the total fit in red. The green line is the continuum level and the dashed maroon line is the residual after subtraction of the fit.

Table 3. Identifications, integrated fluxes, and FWHM of the lines detected in the spectrum of 3C 297.

Line	Wavelength (Å)	Flux $\times 10^{-16}$ (erg cm $^{-2}$ s $^{-1}$)	FWHM (km s $^{-1}$)
Mg II	2797.70	4.23 ± 0.49	1059
O III	3133.70	1.28 ± 0.13	651
[Ne V]	3346.41	2.48 ± 0.30	609
[Ne V]	3426.13	5.92 ± 0.30	595
[O II] broad	3718.94	22.73 ± 0.93	1704
[O II]	3727.11	6.46 ± 0.28	547
[Ne III]	3868.46	8.45 ± 0.39	600
[Ne III]	3968.95	3.97 ± 0.39	585
H δ	4101.34	2.38 ± 0.38	610

NOTE—All lines but Mg II and [O II] broad (see Fig. 6 right panel) are spectroscopically unresolved (the instrumental FWHM is 6.8 Å).

significantly broader (FWHM of 1059 km s^{-1}) than most forbidden lines (FWHM $\sim 500\text{--}600 \text{ km s}^{-1}$) (Osterbrock & Ferland 2006). However, Mg II $\lambda 2798$ is actually a doublet, ($\lambda 2791$ and $\lambda 2798$), and at our spectral resolution the individual components cannot be resolved. With an intrinsic FWHM of 600 km s^{-1} , the Mg II doublet is observed as a broad blended profile.

From the lack of continuum features typical of Type I AGN, and the absence of broad components in the permitted lines, we classify 3C 297 as a Type II radio source.

4.3. Outflowing ionized gas

The broadest feature that we measure in the spectrum of 3C 297 corresponds to a blueshifted component found in the forbidden [O II] $\lambda 3728$ line. This feature is cen-

tered at 3719 Å , with a FWHM of 1790 km s^{-1} . In addition, we also detected a narrow component associated with the same transition, with a FWHM of 547 km s^{-1} , very similar to the width of the remaining narrow forbidden lines (see Figure 6). Because the broad feature is a forbidden line, its origin is outside a putative Broad Line Region (BLR). The gas density in a BLR region is orders of magnitude larger than the critical density of the transition leading to the [O II] $\lambda 3728$ doublet. If the broad component is indeed associated with [O II] $\lambda 3728$, it is displaced by 657 km s^{-1} to the blue of the rest-frame wavelength.

[O III] $\lambda 5007$ falls outside the spectral range of the data. The only published spectrum covering that line is the one of Jackson & Rawlings (1997), that has low spectral resolution ($R = 380$). Although the doublet [O III] $\lambda\lambda 4959, 5007$ is clearly detected, it is not possible to confirm from the Jackson & Rawlings (1997) data the presence of an obvious blueshifted asymmetric line. However, several detections of broad blue-shifted features associated with [O II] have been reported in the literature. For instance, Balmaverde et al. (2016) studied a sample of 224 quasars selected from the Sloan Digital Sky Survey (SDSS) at $z < 1$. They focused on ionized gas outflows traced by the optical [O III] and [O II] lines. Most of the quasar spectra show asymmetries and broad wings in both lines, although the former have larger wings than the latter. These line asymmetries in quasars are generally interpreted as signs of outflows instead of inflows from the farside of the emitting region. Indeed, Perna et al. (2015) detected outflows extending to $\sim 10 \text{ kpc}$ from the central black hole using [O II]. Zakam-

ska & Greene (2014) found that [O II] $\lambda\lambda 3726, 3729$ also shows outflow signatures, in some cases consistent with extremely broad features seen in [O III] (see also Davies et al. (2015)). We conclude that the strong asymmetry observed in [O II] points to an extreme gas outflow in 3C 297. Given the evidence for strong outflows from the spectra, we might expect a disturbed X-ray atmosphere. Even if the number of counts is very low and therefore any statement should be tentative, in the two areas marked with a dashed red circle and ellipse (see Fig. 2), we highlighted an excess of X-ray counts. In the southwestern region (4'' circle) this excess has a Gaussian significance of 5.8σ , while the excess in the north-eastern direction (ellipse 4'' \times 2'') has a significance of $\sim 3.2\sigma$.

4.4. Other sources in the field

As expected, the spectra of the 39 science targets in the field of 3C 297 have different signal-to-noise ratios (S/N). The spectra for those field sources for which we derived a redshift are presented in the Appendix.

Some objects have bright emission lines that are easy to identify (e.g. [O III] for slits 28 and 40, H α for slits 15 and 31). With only four exceptions discussed below, all of our spectra allow the identification of at least two spectral lines, even in those spectra with low S/N.

The redshifts of slits 6, 12, 19, and 42 are derived using the [O II] line only. [O II] is the most probable line observed in these spectra for the following reasons. If it were [O III] ($\lambda 5007$ Å) we would have detected the [O III] ($\lambda 4960$ Å) line as well. If the single line of these four spectra were [Ne III] ($\lambda 3869$ Å), we would always have [O II] and [O III] lines too.

The main conclusion of our field spectroscopy is that we did not identify any galaxies at the same redshift as 3C 297.

5. IS 3C 297 A HIGH-Z FOSSIL GROUP?

Our main findings for 3C 297, namely the presence of an X-ray-luminous hot gas halo and a lack of companion galaxies, would make it a candidate for a so-called fossil group (see, e.g. Ponman et al. 1994; Mendes de Oliveira & Carrasco 2007; Schirmer et al. 2010 and Aguerri et al. 2021 for a recent review).

Fossil groups, or fossil clusters, are systems where the closest M^* galaxies have dynamically collapsed onto the BCG due to dynamic friction (Chandrasekhar 1943), while the group's common X-ray halo would remain visible due to its long cooling time and AGN feedback (Jones et al. 2003). Fossil groups are defined by the presence of an X-ray halo (with $L_X \geq 10^{42}$ erg s $^{-1}$, that is compatible with our estimate, see Sec. 2) and a characteristic magnitude gap of ~ 2 mag between their BCG

and the second-brightest group member (Kundert et al. 2017; Aguerri et al. 2021).

Observationally, catalogs of fossil groups are usually limited to $z < 0.5$. For instance, the highest redshift for the fossil groups reported by a recent survey is $z = 0.442$ (Johnson et al. 2018). In the Hess et al. (2012) sample, the highest-redshift fossil group is 0.489. Voevodkin et al. (2010) presented an X-ray-selected sample of X-ray-luminous fossil groups at $z < 0.2$. Pratt et al. (2016) studied four very X-ray-luminous fossil groups detected in the Planck Sunyaev-Zeldovich Survey whose temperatures are 5-6 keV with total masses exceeding $10^{14} M_\odot$.

Simulations show that a fossil system may assemble half of its mass in dark matter by redshift $z > 1$, and that the assembled mass at any redshift is generally higher in a fossil groups than in regular groups (Dariush et al. 2007). The existence of a fossil group at the redshift of 3C 297 is therefore compatible with theoretical expectations.

High-redshift examples of fossil groups are very limited with current record holders standing at $z=0.47$ (Yoo et al. 2021) and $z=0.7$ (Grillo et al. 2013). The fact that we did not find physical companion galaxies makes 3C 297 one of the highest redshift fossil groups known to date.

Hess et al. (2012), using both SDSS and VLA data, demonstrated that fossil groups host radio-loud AGN detected at 1.4 GHz. 3C 297, being a stronger source than the AGN in the sample studied by Hess et al. (2012), shows that fossil groups can also host powerful radio sources. We want to highlight that, as reported in Lotz et al. (2008), time-scales of galaxy mergers are of the order of 1 Gyr. Even if poorly constrained, 3C 297 has a cooling time longer than 1 Gyr.

6. SUMMARY AND CONCLUSIONS

We have presented an optical/X-ray study of the high-redshift ($z=1.408$) quasar 3C 297. In the 3C *Chandra* Snapshot observation, we observed a complex morphology of the X-ray halo and the detection of the X-ray counterpart of the radio hotspot visible in the VLA image at 8.4 GHz. With new deeper *Chandra* observations, we performed the spectral analysis of the bright X-ray hotspot and of the nuclear region. The nucleus is not detected in the radio image. Therefore, we used a tentative position obtained from an available spectral index map. We obtained an X-ray luminosity of $L_X = 2.82^{+0.57}_{-0.46} \times 10^{44}$ erg s $^{-1}$ for the hotspot and $L_X = 1.15^{+0.53}_{-0.40} \times 10^{44}$ erg s $^{-1}$ for the nucleus, in the energy range 0.5-7 keV. We also investigated if the extended X-ray emission, not spherically symmetric, as expected for cluster emission, had a thermal or nonthermal origin, i.e. if it was due to the

hot gas or to IC/CMB. We have only been able to put an upper bound on the temperature being 6 keV. Given the distribution of the surrounding X-ray gas, suggesting that 3C 297 could be the BCG of a galaxy cluster or group, we searched for fainter companions/galaxy members. With new GMOS observations, we have obtained optical spectra of the neighboring sources of our target, and for 19 of them we measured their redshift. The main conclusion of our field spectroscopy is that we did not identify any galaxies at the same redshift as 3C 297. We therefore postulate that 3C 297 is a fossil group, being the first at such high redshift. From the optical spectral analysis, we observed that the line profile displays a broad, prominent blue asymmetry, indicating the presence of powerful ionized gas outflows in the center of the radio galaxy.

We thank the anonymous referee for constructive comments on the original manuscript. We want to thank W. R. Forman for fruitful discussion and extremely useful comments and suggestions. This study is based on observations obtained at the Gemini Observatory which is operated by AURA under a cooperative agreement with the NSF on behalf of the Gemini partnership. With heartfelt thanks to the Gemini observatory staff that obtained our data and helped us with the data reduction during the challenging conditions of a global pandemic: Germán Gimeno, Kristin Chiboucas, Joan Font-Serra, Jennifer Berghuis, José Cortes, Ted Rudyk, Lindsay Magill, and Javier Fuentes.

The authors wish to recognize and acknowledge the very significant cultural role and reverence that the sum-

mit of Mauna Kea has always had within the indigenous Hawaiian community. We are most fortunate to have the opportunity to obtain astronomical observations from this mountain.

Support for this work was provided by the National Aeronautics and Space Administration (NASA) through Chandra grants GO1-22112B, GO9-20083X, GO0-21110X and GO1-22087X. The National Radio Astronomy Observatory is a facility of the National Science Foundation operated under cooperative agreement by Associated Universities, Inc. SAO Image DS9 development has been made possible by funding from the Chandra X-ray Science Center (CXC), the High Energy Astrophysics Science Archive Center (HEASARC) and the JWST Mission office at Space Telescope Science Institute (Joye & Mandel 2003).

R.K. acknowledges support from the Smithsonian Institution and the Chandra High Resolution Camera Project through NASA contract NAS8-03060.

A.R.A. acknowledges CNPq (grant 312036/2019-1) for partial support to this work.

C.S. acknowledges support from the MIUR grant FARE “SMS”.

Software: : Astropy (Astropy et al. 2013), CIAO (Fruscione et al. 2006), Matplotlib (Hunter 2007), Numpy (Van Der Walt et al. 2011), Sherpa (Freeman et al. 2001).

Facilities: Gemini, Chandra.

REFERENCES

- Aguerri, J. A. L. & Zarattini, S. 2021, *Universe*, 7, 132. doi:10.3390/universe7050132
- The Astropy Collaboration, Robitaille, T. P., Tollerud, E. J., et al. 2013, *A&A*, 558, A33. doi: 10.1051/0004-6361/201322068
- Balmaverde, B., Marconi, A., Brusa, M., et al. 2016, *A&A*, 585, A148. doi:10.1051/0004-6361/201526694
- Begelman, M. C., Blandford, R. D., & Rees, M. J. 1984, *Reviews of Modern Physics*, 56, 255. doi:10.1103/RevModPhys.56.255
- Bennett, A. S. 1962a, *MmRAS*, 68, 163. adsurl:https://ui.adsabs.harvard.edu/abs/1962MmRAS..68..163B
- Bennett, A. S. 1962b, *MNRAS*, 125, 75. doi:10.1093/mnras/125.1.75
- Bennett, C. L., Larson, D., Weiland, J. L., et al. 2014, *ApJ*, 794, 135. doi:10.1088/0004-637X/794/2/135
- Best, P. N., von der Linden, A., Kauffmann, G., et al. 2007, *MNRAS*, 379, 894. doi:10.1111/j.1365-2966.2007.11937.x
- Blandford, R., Meier, D., & Readhead, A. 2029, *ARA&A*, 57, 467. doi:10.1146/annurev-astro-081817-05194
- Bykov, A. M., Churazov, E. M., Ferrari, C., et al. 2015, *SSRv*, 188, 141. doi:10.1007/s11214-014-0129-4
- Cardelli, J. A., Clayton, G. C., Mathis, J. S. 1989, *ApJ*, 345, 245. doi:10.1086/167900
- Chandrasekhar, S. 1943, *ApJ*, 97, 255. doi:10.1086/144517
- Chiaberge, M., Gilli, R., Lotz, J. M., et al. 2015, *ApJ*, 806, 147. doi:10.1088/0004-637X/806/2/147
- Churazov, E., Brüggen, M., Kaiser, C. R., et al. 2001, *ApJ*, 554, 261. doi:10.1086/321357
- Cooke, B. A., Lawrence, A., & Perola, G. C. 1978, *MNRAS*, 182, 661. doi:10.1093/mnras/182.4.661

- Dariush, A., Khosroshahi, H. G., Ponman, T. J., et al. 2007, *MNRAS*, 382, 433. doi:10.1111/j.1365-2966.2007.12385.x
- Davies, R., Schirmer, M., & Turner, J. E. H. 2015, *MNRAS*, 449, 1731. doi:10.1093/mnras/stv343
- de Gasperin, F., Orrú, E., Murgia, M., et al. 2012, *A&A*, 547, A56. doi:10.1051/0004-6361/201220209
- Event Horizon Telescope Collaboration, et al., 2019, *ApJL*, 875, L4. doi:10.3847/2041-8213/ab0ec7
- Fabian, A. C. 2012, *ARA&A*, 50, 455. doi:10.1146/annurev-astro-081811-125521
- Felten, J. E. & Rees, M. J. 1969, *Nature*, 221, 924. doi:10.1038/221924a0
- Forman, W., Jones, C., Churazov, E., et al. 2007, *ApJ*, 665, 1057. doi:10.1086/519480
- Freeman, P., Doe, S., & Siemiginowska, A. 2001, *Proc. SPIE*, 4477, 76. doi:10.1117/12.447161
- Fruscione, A., McDowell, J. C., Allen, G. E., et al. 2006, *Proc. SPIE*, 6270, 62701V. doi:10.1117/12.671760
- Ghisellini, G., Celotti, A., Tavecchio, F., et al. 2014, *MNRAS*, 438, 2694. doi:10.1093/mnras/stt2394
- Ghisellini, G., Tavecchio, F., Maraschi, L., et al. 2014, *Nature*, 515, 376. doi:10.1038/nature13856
- Ghisellini, G., Haardt, F., Ciardi, B., et al. 2015, *MNRAS*, 452, 3457. doi:10.1093/mnras/stv1541
- Glazebrook, K. & Bland-Hawthorn, J. 2001, *PASP*, 113, 197. doi:10.1086/318625
- Grillo, C., Christensen, L., Gallazzi, A. et al. 2013, *MNRAS*, 433, 2604. doi:10.1093/mnras/stt930
- Harris, D. E. & Grindlay, J. E. 1979, *MNRAS*, 188, 25. doi:10.1093/mnras/188.1.25
- Hilbert, B., Chiaberge, M., Kotyla, J. P. et al., 2016, *ApJSS*, 225, 12. doi:10.3847/0067-0049/225/1/12
- Hess, K. M., Wilcots, E. M., & Hartwick, V. L. 2012, *AJ*, 144, 48. doi:10.1088/0004-6256/144/2/48
- HI4PI Collaboration, Ben Bekhti, N., Flöer, L., et al. 2016, *A&A*, 594, A116. doi:10.1051/0004-6361/201629178
- Hook, I. M., Jørgensen, I., Allington-Smith, J. R., et al. 2004, *PASP*, 116, 425. doi:10.1086/383624
- Hunter, J. D. 2007, *Computing in Science & Engineering*, 9, 90. doi:10.1109/MCSE.2007.55
- Jackson, N. & Rawlings, S. 1997, *MNRAS*, 286, 241. doi:10.1093/mnras/286.1.241
- Johnson, L. E., Irwin, J. A., White, R. E., et al. 2018, *ApJ*, 869, 170. doi:10.3847/1538-4357/aaf00b
- Joye, W. A. & Mandel, E. 2003, *adass*, 295, 489. [adsurl:https://ui.adsabs.harvard.edu/abs/2003ASPC..295..489J](https://ui.adsabs.harvard.edu/abs/2003ASPC..295..489J)
- Jones, L. R., Ponman, T. J., Horton, A., et al. 2003, *MNRAS*, 343, 627. doi:10.1046/j.1365-8711.2003.06702.x
- Kotyla, J. P., Chiaberge, M., Baum, S., et al. 2016, *ApJ*, 826, 46. doi:10.3847/0004-637X/826/1/46
- Kraft, R. P., Birkinshaw, M., Nulsen, P. E. J., et al. 2012, *ApJ*, 749, 19. doi:10.1088/0004-637X/749/1/19
- Kundert, A., D'Onghia, E., & Aguerri, J. A. L. 2017, *ApJ*, 845, 45. doi:10.3847/1538-4357/aa7b88
- Lynden-Bell, D. 1969, *Nature*, 223, 690. doi:10.1038/223690a0
- Lotz, J. M., Jonsson, P., Cox, T. J., et al. 2008, *MNRAS*, 391, 1137. doi:10.1111/j.1365-2966.2008.14004.x
- Madrid, J. P., Donzelli, C. J., Rodríguez-Ardila, A., et al. 2018, *ApJS*, 238, 31. doi:10.3847/1538-4365/aade8f
- Massaro, F., Harris, D. E., Chiaberge, M., et al. 2009, *ApJ*, 696, 980. doi:10.1088/0004-637X/696/1/980
- Massaro, F., Harris, D. E., Tremblay, G. R., et al. 2010, *ApJ*, 714, 589. doi:10.1088/0004-637X/714/1/589
- Massaro, F. & Ajello, M. 2011, *ApJL*, 729, L12. doi:10.1088/2041-8205/729/1/L12
- Massaro, F., Harris, D. E., Liuzzo, E., et al. 2015, *ApJS*, 220, 5. doi:10.1088/0067-0049/220/1/5
- Massaro, F., Missaglia, V., Stuardi, C., et al. 2018, *ApJS*, 234, 7. doi:10.3847/1538-4365/aa8e9d
- Mendes de Oliveira, C. L., & Carrasco, E. R. 2007, *ApJ*, 670, L93. doi:10.1086/524408
- Merloni, A. & Heinz, S. 2013, *Planets, Stars and Stellar Systems. Volume 6: Extragalactic Astronomy and Cosmology*, 503. doi:10.1007/978-94-007-5609-0_11
- Morganti, R., Oosterloo, T., Tadhunter, C. N., et al. 1999, *Astronomy & Astrophysics Supplement*, 140, 355. doi:10.1051/aas:1999427
- Osterbrock, D. E. & Ferland, G. J. 2006, *Astrophysics of gaseous nebulae and active galactic nuclei*, 2nd. ed. by D.E. Osterbrock and G.J. Ferland. Sausalito, CA: University Science Books, 2006. [adsurl:https://ui.adsabs.harvard.edu/abs/2006agna.book.....O](https://ui.adsabs.harvard.edu/abs/2006agna.book.....O)
- Owen, F. N., Eilek, J. A., & Kassim, N. E. 2000, *ApJ*, 543, 611. doi:10.1086/317151
- Padovani, P., Alexander, D. M., Assef, R. J., et al. 2017, *A&A Rv*, 25, 2. doi:10.1007/s00159-017-0102-9
- Paterno-Mahler, R., Blanton, E. L., Brodwin, M., et al. 2017, *ApJ*, 844, 78. doi:10.3847/1538-4357/aa7b89
- Perley, R. A. & Meisenheimer, K. 2017, *A&A*, 601, A35. doi:10.1051/0004-6361/201629704
- Perna, M., Brusa, M., Cresci, G., et al. 2015, *A&A*, 574, A82. doi:10.1051/0004-6361/201425035
- Ponman, T. J., Allan, D. J., Jones, L. R., et al. 1994, *Nature*, 369, 462. doi:10.1038/369462a0
- Pratt, G. W., Pointecouteau, E., Arnaud, M., et al. 2016, *A&A*, 590, L1. doi:10.1051/0004-6361/201628462
- Rees, M. J., Sciamia, D. W., & Setti, G. 1968, *Nature*, 217, 326. doi:10.1038/217326a0

- Rees, M. J. 1984, *ARA&A*, 22, 471.
doi:10.1146/annurev.aa.22.090184.002351
- Rosati, P., Borgani, S., & Norman, C. 2002, *ARA&A*, 40, 539. doi:10.1146/annurev.astro.40.120401.150547
- Salpeter, E. E. 1964, *ApJ*, 140, 796. doi:10.1086/147973
- Schirmer, M., Suyu, S., Schrabback, T., et al. 2010, *A&A*, 514, A60. doi:10.1051/0004-6361/200913810
- Schlafly, E. F., Finkbeiner, D. P. 2011, *ApJ*, 737, 103. doi: 10.1088/0004-637X/737/2/103
- Spinrad, H., Djorgovski, S., Marr, J., & Aguilar, L. 1985, *PASP*, 97, 932. doi: 10.1086/131647
- Stuardi, C., Missaglia, V., Massaro, F., et al. 2018, *ApJS*, 235, 32. doi: 10.3847/1538-4365/aaafcf
- Van Der Walt, S., Colbert, S. C., & Varoquaux, G. 2011, *Computing in Science & Engineering*, 13, 22. doi: 10.1109/MCSE.2011.37
- Voevodkin, A., Borozdin, K., Heitmann, K., et al. 2010, *ApJ*, 708, 1376. doi:10.1088/0004-637X/708/2/1376
- Volonteri, M., Haardt, F., Ghisellini, G., et al. 2011, *MNRAS*, 416, 216. doi:10.1111/j.1365-2966.2011.19024.x
- Wing, J. D. & Blanton, E. L. 2011, *AJ*, 141, 88. doi:10.1088/0004-6256/141/3/88
- Yoo, J., Ko, J. Kim, J-W., et al. 2021, *MNRAS*, 508, 2634. doi: 10.1093/mnras/stab2707
- Yuan, W., Fabian, A. C., Celotti, A., et al. 2003, *MNRAS*, 346, L7. doi:10.1046/j.1365-2966.2003.07234.x
- Zakamska, N. L. & Greene, J. E. 2014, *MNRAS*, 442, 784. doi: 10.1093/mnras/stu842

APPENDIX

This appendix presents the new Gemini spectra of the 19 galaxies for which we derived a redshift.

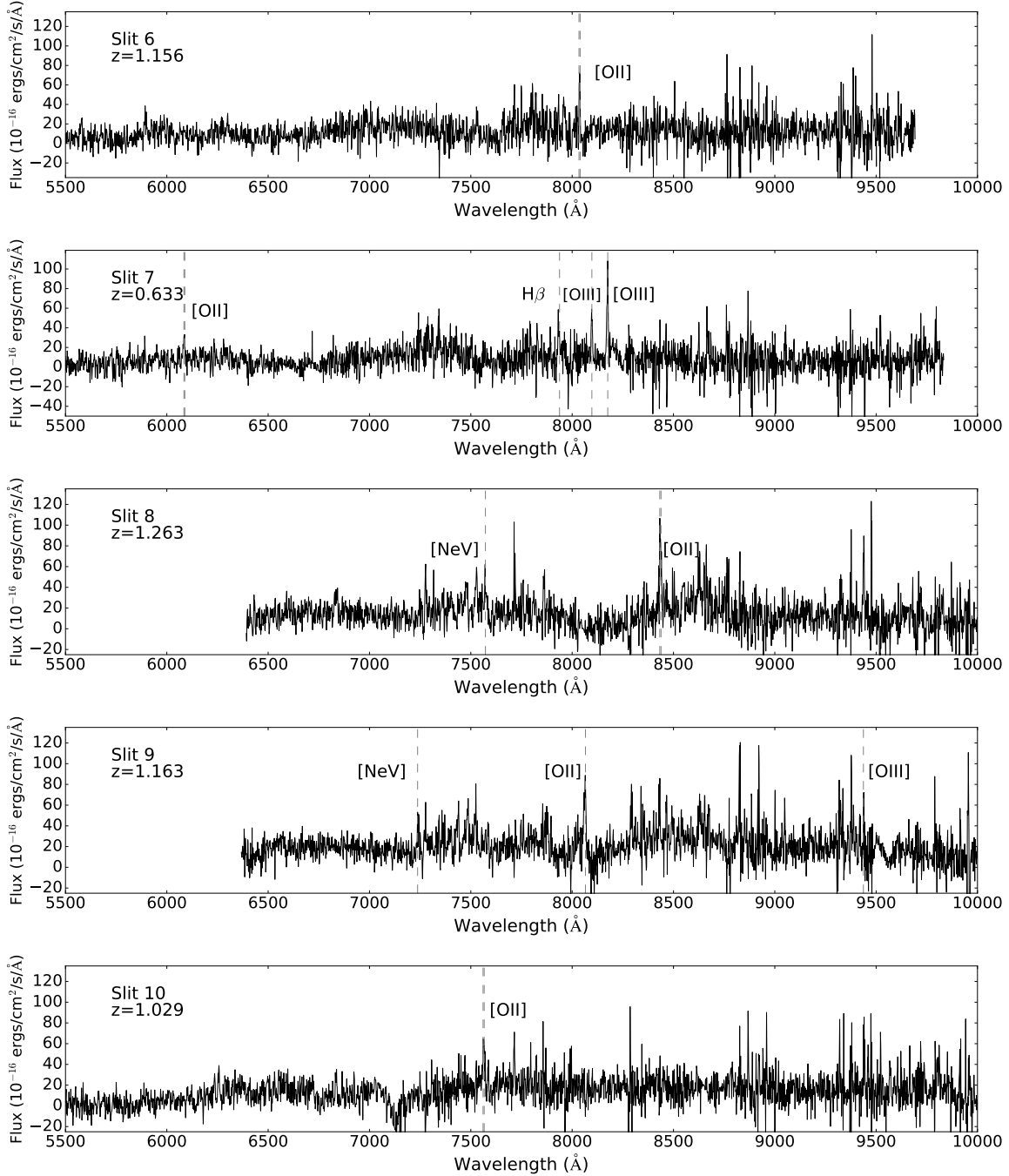


Figure 7. New GMOS spectra of targets in the 3C 297 field. All spectra are shown in the observed wavelength. The dashed vertical lines mark emission lines that were identified visually. Other apparently significant but non-marked lines are due to noise, which cannot be discerned from real lines at the resolution chosen for these plots.

Figure 8. New GMOS spectra of targets in the 3C297 field. All spectra are shown in the observed wavelength. The dashed vertical lines mark emission lines that were identified visually. Other apparently significant but non-marked lines are due to noise, which cannot be discerned from real lines at the resolution chosen for these plots.

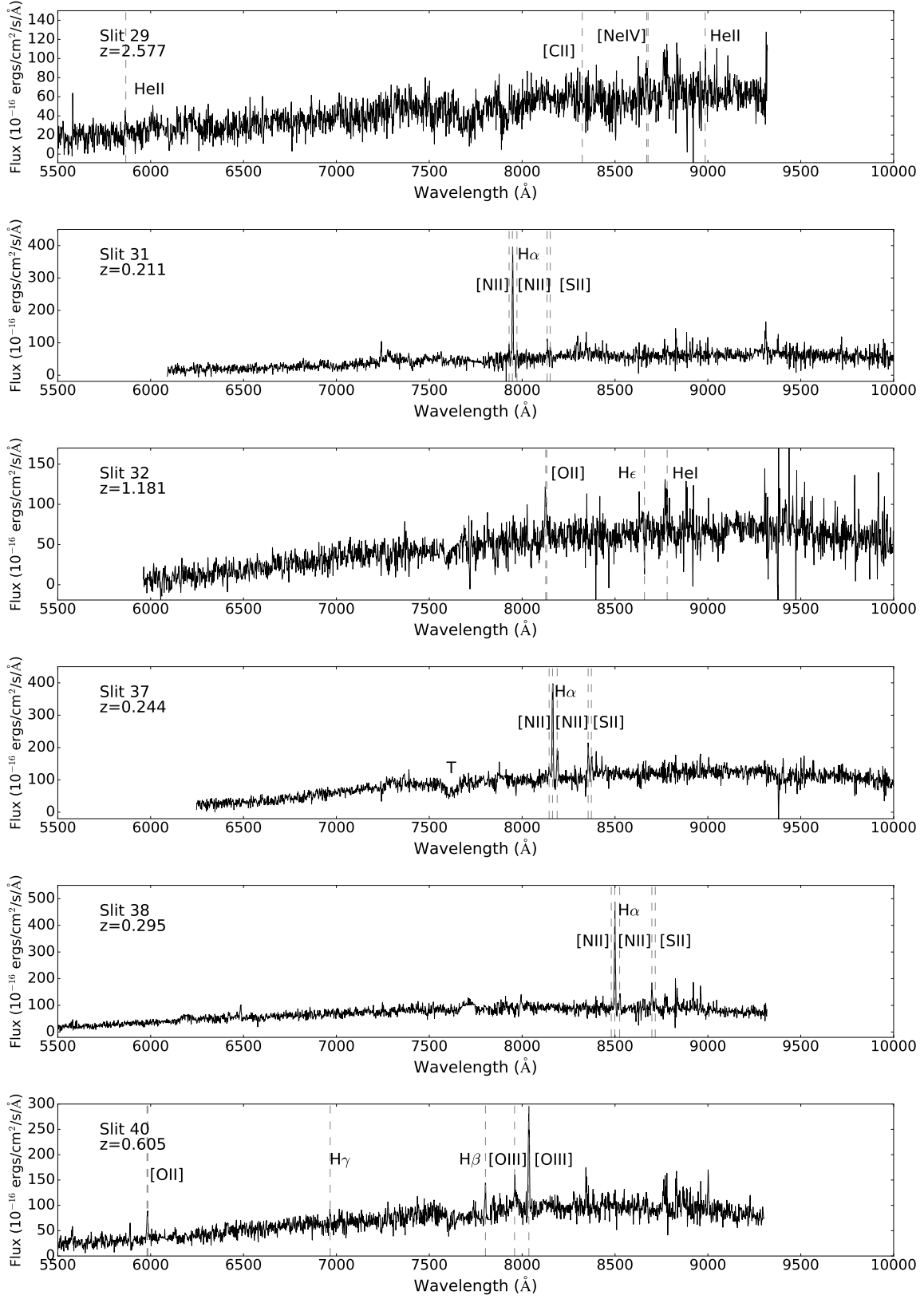


Figure 9. New GMOS spectra of targets in the 3C 297 field. All spectra are shown in the observed wavelength. The dashed vertical lines mark emission lines that were identified visually. Other apparently significant but non-marked lines are due to noise, which cannot be discerned from real lines at the resolution chosen for these plots.

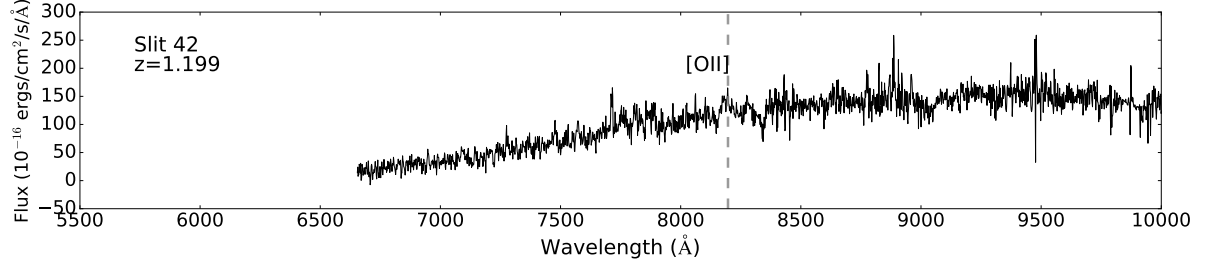


Figure 10. New GMOS spectra of targets in the 3C 297 field. All spectra are shown in the observed wavelength. The dashed vertical lines mark emission lines that were identified visually. Other apparently significant but non-marked lines are due to noise, which cannot be discerned from real lines at the resolution chosen for these plots.